Nano Research

ISSN 1998-0124 CN 11-5974/O4
https://doi.org/10.1007/s12274-023-5581-6

Research Article

Immunogenic cell death effects induced by doxorubicin improved chemo-immunotherapy via restoration of granzyme B activity

Tao Huang[1,§], Xiaofan Sun[1,§], Yingqiu Qi[1,2,§], Xi Yang[1], Linyao Fan[1], Mengdie Chen[2], Yale Yue[2], Hong Ge[3], Yiye Li[4], Guangjun Nie[4] (✉), Huan Min[1,2] (✉), and Xianfu Sun[1] (✉)

[1] *Department of Breast Disease, The Affiliated Cancer Hospital of Zhengzhou University & Henan Cancer Hospital, Henan Institute of Advanced Technology, Zhengzhou University, Zhengzhou 450008, China*
[2] *Department of Pharmacology, School of Basic Medical Sciences, Zhengzhou University, Zhengzhou 450001, China*
[3] *Department of Radiation Oncology, The Affiliated Cancer Hospital of Zhengzhou University & Henan Cancer Hospital, Zhengzhou 450003, China*
[4] *CAS Key Laboratory for Biomedical Effects of Nanomaterials and Nanosafety & CAS Center for Excellence in Nanoscience, National Center for Nanoscience and Technology, Beijing 100190, China*
[§] *Tao Huang, Xiaofan Sun, and Yingqiu Qi contributed equally to this work.*

Received: 10 January 2023 / **Revised:** 14 February 2023 / **Accepted:** 14 February 2023

ABSTRACT

Chemotherapy remains one of the irreplaceable treatments for cancer therapy. The use of immunogenic cell death (ICD)-inducing chemotherapeutic drugs offers a practical strategy for killing cancer cells, simultaneously eliciting an antitumor immune response by promoting the recruitment of cytotoxic immune cells and production of granzyme B (GrB). However, numerous malignant cancers adaptively acquired the capacity of secreting serpinb9 (Sb9), a physiological inhibitor of GrB, which can reversibly inhibit the biological activity of GrB. To circumvent this dilemma, in this study, an integrated tailor-made nanomedicine composed of tumor-targeting peptide (Arg-Gly-Asp, RGD) decorated liposome, doxorubicin (DOX, an effective ICD inducer), and the compound 3034 (an inhibitor of Sb9), is developed (termed as D3RL) for breast cancer chemo-immunotherapy. *In vitro* and *in vivo* studies show that D3RL can directly kill tumor cells and trigger the host immune response by inducing ICD. Meanwhile, D3RL can competitively relieve the inhibition of Sb9 to GrB. The restored GrB can not only effectively induce tumor immunotherapy, but also degrade matrix components in the tumor microenvironment, consequently improving the infiltration of immune cells and the penetration of nanomedicines, which in return enhance the combined antitumor effect. Taken together, this work develops an integrated therapeutic solution for targeted production and restoration of GrB to achieve a combined chemo-immunotherapy for breast cancer.

KEYWORDS

immunogenic cell death, granzyme B, serpinb9, chemo-immunotherapy, nanomedicine

1 Introduction

Breast cancer is the most common malignancy in women with more than two million incidences worldwide each year [1, 2]. Among the emerging approved therapeutic modalities, chemotherapy remains one of the irreplaceable treatments for breast cancer [3, 4]. Clinical and preclinical researches show that some chemotherapeutic drugs (such as platinum and anthracycline) can not only directly kill tumor cells, but also induce immunogenic cell death (ICD) [5–7]. Tumor cells suffering from ICD up-regulate levels of damage-associated molecular patterns (DMAPs), which enable dendritic cells (DCs) to phagocytose those damaged tumor cells and present tumor antigen epitopes, consequently promoting the activation of DCs and triggering a specific response of host immunity [8–10]. The activated host immune system can recruit cytotoxic T lymphocytes and natural killer (NK) cells to induce apoptosis of tumor cells by locally releasing perforin and granzyme B (GrB), leading to an effective immune-killing to tumor tissues [11, 12]. Thus, the use of ICD-inducing chemotherapeutic drugs offers a practical strategy for killing cancer cells while simultaneously eliciting an antitumor immune response.

Emerging shreds of evidence have verified that many malignant tumors (including breast cancer and lung cancer) adaptively acquired the capacity to secrete serpinb9 (Sb9), a physiological inhibitor of GrB, which can reversibly form a protein complex with GrB to inhibit its biological activity on immune killing [13–15]. Moreover, Sb9 can also inhibit the degradation of tumor extracellular matrix by GrB, consequently maintaining the matrix density of the tumor microenvironment, which limits the penetration of therapeutic drugs and provides a basis for drug resistance [16, 17]. Therefore, blocking the inhibitory effect of Sb9 on GrB is a promising strategy for oncotherapy. Encouragingly, Reza Abdi and colleagues demonstrated that knocking out the Sb9 protein can significantly improve the infiltration of GrB-positive immune cells in tumor tissue, and effectively inhibit the growth of tumors [18]. Furthermore, they have screened out a compound, 1,3-benzoxazole-6-carboxylic acid (denoted as 3034) as an

Address correspondence to Guangjun Nie, niegj@nanoctr.cn; Huan Min, minh@zzu.edu.cn; Xianfu Sun, zlyysunxianfu1256@zzu.edu.cn

inhibitor of Sb9, which can competitively bind with Sb9 to restore the level of GrB, as well as its biological activity on tumor-killing. However, systematic administration of 3034 may result in early activation of GrB at an immune-exempt tissue, leading to severe autoimmune diseases [19]. Therefore, targeted delivery of 3034 to the tumor site is a promising strategy to boost the therapeutic effect of GrB in a safe manner.

Recent studies have shown promising preclinical results of antitumor immune responses induced by doxorubicin (DOX) due to its ICD-inducing properties [20, 21]. Unfortunately, DOX indiscriminately damages both tumor cells and normal cells following systematic administration and exhibits dose-dependent cardiotoxicity [22]. Considering the challenges and the positive correlation between DOX-inducing ICD and 3034-mediated GrB relieving, we propose that targeted codelivery of DOX and 3034 may achieve a synergistic chemo-immunotherapy, a hypothesis that has not been explored so far.

Herein, an integrated tailor-made nanomedicine composed of tumor-targeting peptide Arg-Gly-Asp (RGD) decorated liposome, hydrophilic doxorubicin hydrochloride, and hydrophobic compound 3034 is developed (termed as D3RL) for breast cancer chemo-immunotherapy. The proposed antitumor mechanism of D3RL is illustrated in Scheme 1. The prepared D3LR targets and accumulates at the tumor site owing to the affinity of decorated RGD peptide to integrin $\alpha_v\beta_3$ overexpressed in tumor cells [23, 24]. The released DOX can directly kill tumor cells and trigger the host immune response by inducing ICD. The activated immune system recruits cytotoxic immune cells to kill tumor cells by releasing GrB. Meanwhile, the locally released 3034 can competitively bind with Sb9, consequently relieving the inhibition of Sb9 to GrB. The restored GrB can not only effectively induce tumor immunotherapy, but also degrade matrix components in the tumor microenvironment, consequently improving the infiltration of immune cells and the penetration of nanomedicines, which in return enhances the combined antitumor effect. This work proposes an integrated therapeutic solution for the targeted production and restoration of GrB to boost the chemo-immunotherapy for breast cancer.

2 Results and discussion

2.1 Synthesis and characterization of D3RL

The RGD peptide-conjugated amphiphilic polymer 1,2-distearoyl-sn-glycero-3-phosphoethanol-amine-N-[methoxy(polyethylene glycol)] (DSPE-PEG), denoted as DSPE-PEG-RGD, was synthesized using the Michael addition reaction according to a published method [25], and successful synthesis was confirmed by mass spectrum analysis (Fig. S1 in the Electronic Supplementary Material (ESM)). DOX-loaded liposome (DL), 3034-loaded liposome (3L), and DOX/3034-coloaded liposomes (D3L) were fabricated using a modified thin-film dispersion method [26], where the DOX was trapped in the hydrophilic core and the 3034 was inserted into the hydrophobic layer. In order to endow the nanomedicine with the capacity of tumor targeting, the DSPE-PEG-RGD was used instead of DSPE-PEG with a similar protocol, and the obtained nanomedicine was denoted as DOX-3034-RGD-Lipo (D3RL). To optimize the drug loading capacity, different mass ratios of drug/liposome were evaluated, and the loaded 3034 or DOX was quantitatively analyzed with high-performance liquid chromatography (HPLC). As shown in Fig. S2 in the ESM, the loading efficiency (LE) of both DOX and 3034 decreased with the mass ratio of drug/liposome, while the encapsulation efficiency (EE) increased with this mass ratio. The optimized LE of DOX and 3034 were 1.3% and 4.5%, and EE of DOX and 3034 were 61.2% and 43.1%, respectively, when the mass ratio of drug/liposome was set as 1:8, which gave an approximate molar ratio of 1:3.5 for DOX and 3034 in the prepared D3RL. The successful drug loading of 3034 and DOX was also confirmed with ultraviolet–visible (UV–vis) spectra (Fig. S3 in the ESM), where the prepared D3L and D3RL exhibited the typical absorption peaks of 3034 (located at 300 nm) and DOX (located at 488 nm). Transmission electron microscopy (TEM) images revealed uniform spherical morphologies of the D3RL and other nanomedicines (Fig. 1(a) and Fig. S4(a) in the ESM). Dynamic light scattering (DLS) results showed that the hydrodynamic size of D3RL was ~ 137.87 nm, with a polydispersity index (PDI) of 0.20 (Fig. 1(b)). The hydrodynamic size and surface charge of these nanomedicines used in the following experiments were characterized and summarized in Fig. S4(b) and Table S1 in the ESM. Furthermore, there were no significant changes in hydrodynamic size and zeta potential after incubation in phosphate buffer saline (PBS) at 4 °C for 7 days, indicating the excellent colloidal stability of prepared D3L and D3RL (Fig. S5 in the ESM). Next, the drug release profile of D3RL was studied at pH 6.5 or 7.4. As shown in Figs. 1(c) and 1(d), both DOX and 3034 showed sustained release profiles within 24 h and exhibited slightly higher release rates at pH 6.5 than pH 7.4, which was favorable for drug release in the acidic tumor microenvironment [27, 28].

2.2 Cellular uptake of D3RL

Considering the specific affinity to integrin $\alpha_v\beta_3$, which is overexpressed in numerous tumor cells [29, 30], RGD peptide decoration was used to enhance the cellular uptake of prepared D3RL in this work. As shown in Fig. 1(e), after incubated with different nanomedicines containing DOX for 4 h, abundant red fluorescence signals separated around the cellular nuclear, suggesting the effective uptake of prepared nanomedicines by luciferase-expressing 4T1 (4T1-Luc) cells. Notably, there is an obviously brighter red fluorescence in cells treated with D3RL, compared with that treated with D3L. The enhanced cellular uptake was further confirmed by quantitative analysis using flow cytometry (Figs. 1(f) and 1(g)), where a significantly higher DOX signal was detected in D3RL-treated cells compared with other groups, indicating the facilitation of RGD decoration to cellular uptake.

2.3 ICD inducing and GrB restoring by D3RL

The cytotoxicity of the prepared nanomedicines was investigated using the cell counting kit-8 (CCK-8) assay. Free 3034 and 3034-loaded liposomes did not exhibit significant cytotoxicity in 4T1-Luc cells, even at a concentration up to 64 μg/mL, which was much higher than the dose used in the following experiments (Fig. S6(a) in the ESM). In contrast, Free DOX and DOX-containing nanomedicines showed dose-dependent toxicity to 4T1-Luc cells. Notably, compared with D3L, the D3RL exhibited a much lower IC_{50} (half maximal inhibitory concentration) value (5.1 vs. 9.6 μg/mL), which is comparable to free DOX with an IC_{50} of 4.1 μg/mL (Fig. S6(b) in the ESM). The excellent cytotoxicity of D3RL may be attributed to the enhanced cellular uptake from RGD decoration.

As a traditional anthracycline-based chemotherapeutic drug, DOX has been well-recognized to induce an immunological response through ICD effect. During induction of ICD effect, exposure of calreticulin (CRT) and release of high-mobility group box 1 (HMGB1) and adenosine triphosphate (ATP) are recognized as “eat me” and “danger” signals for DC activation [8–10]. We next investigated whether the prepared D3RL could induce the ICD effect in 4T1-Luc cells. As shown in Fig. 2(a), the

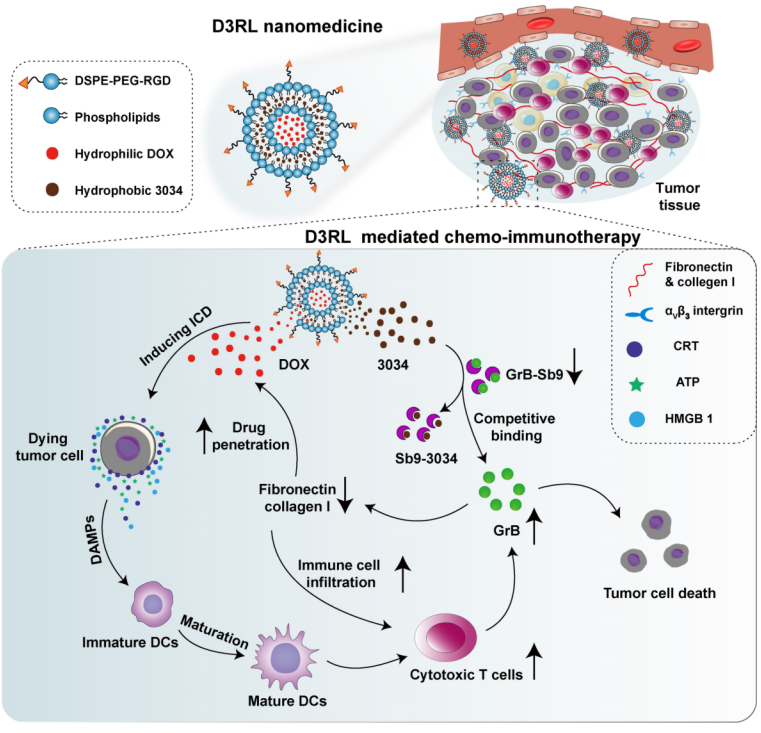

Scheme 1 Schematic illustration of D3RL mediated tumor chemo-immunotherapy. The prepared D3RL can target the tumor tissue by virtue of the decorated RGD peptide. The released DOX can induce the ICD effect of tumor cells, subsequently promoting the maturation of DCs and recruitment of cytotoxic T cells, which enhanced the production of GrB. Meanwhile, the locally released 3034 can competitively bind with Sb9 to relieve the inhibition of Sb9 to GrB. The restored GrB can not only effectively induce the tumor immunotherapy, but also degrade the matrix components (such as fibronectin and collagen I) in the tumor microenvironment, consequently improving the infiltration of immune cells and the penetration of nanomedicines, which in return enhanced the combined antitumor effect.

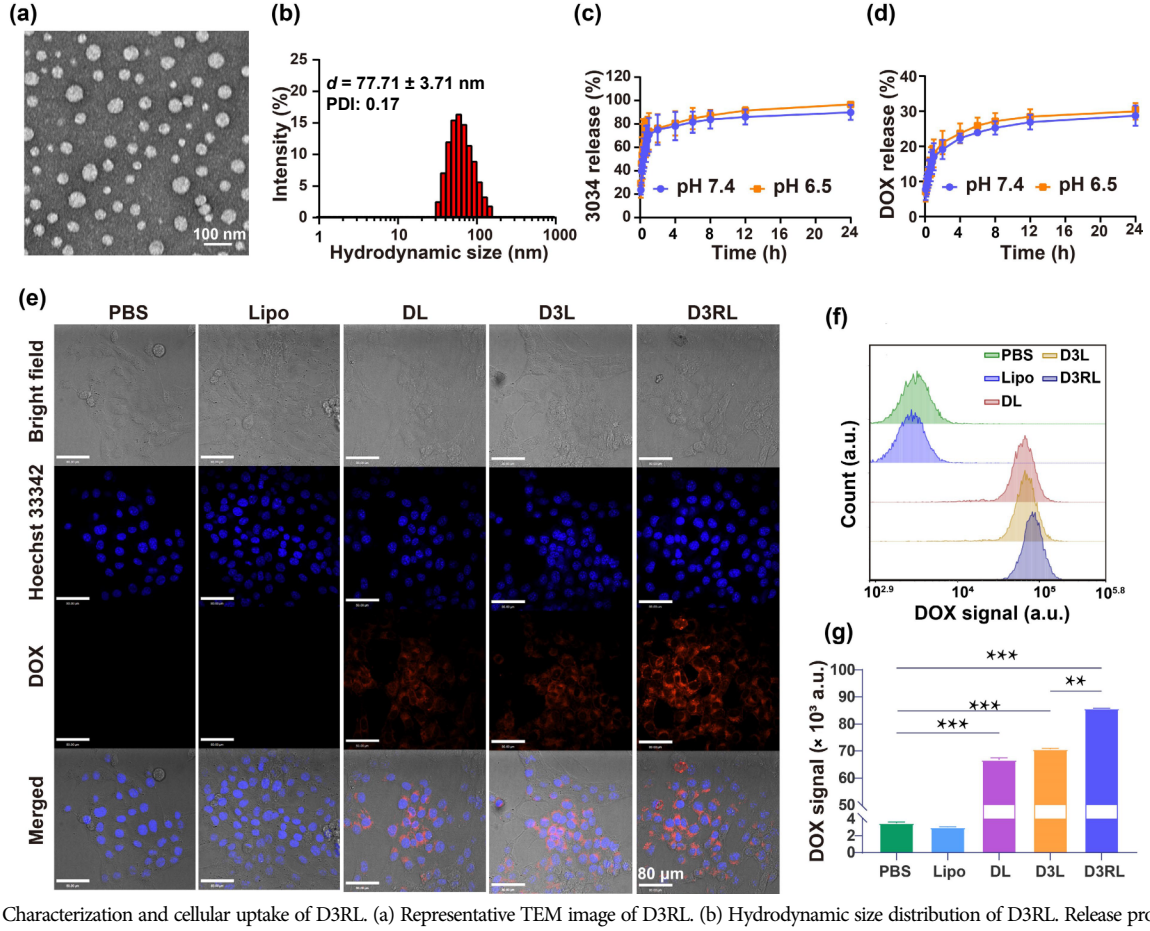

Figure 1 Characterization and cellular uptake of D3RL. (a) Representative TEM image of D3RL. (b) Hydrodynamic size distribution of D3RL. Release profiles of (c) 3034 and (d) DOX from prepared D3RL at pH 7.4 or 6.5. (e) Confocal laser scanning microscope images of 4T1-Luc cells treated with indicated nanomedicines. Cell nuclei were stained with Hoechst 33342 (blue), and the nanomedicines were self-labeled with DOX (red). Scale bar, 80 μm. (f) Flow cytometry and (g) quantitative analysis of DOX signal in 4T1-Luc cells with different treatments. Data were analyzed by GraphPad Prism software. Student's *t*-test was performed for the statistical analysis of the two groups. Data are shown as mean ± s.d. ($n = 3$). **, $p < 0.01$; ***, $p < 0.001$.

DOX-containing nanomedicines can obviously stimulate the cellular exposure of CRT, and the quantitative flow cytometry analysis further confirmed this result (Figs. 2(b) and 2(c)). In addition, the robust up-regulation of HMGB1 and ATP induced by DOX-containing nanomedicines was verified by fluorescence imaging (Fig. 2(d)) and quantitative analysis with an enzyme-linked immunosorbent assay (ELISA) kit, respectively (Figs. 2(e) and 2(f)). Notably, compared with DL and D3L, D3RL treatment can significantly enhance all these DMAPs exposures in 4T1-Luc cells, which may be attributed to the enhanced cellular internalization from RGD decoration. Above all, the prepared nanomedicine D3RL retained an excellent capacity for ICD inducing.

It has been demonstrated that some malignant cancer cells endogenously produced GrB, which is reversibly silenced by Sb9 in the form of the Sb9-GrB complex [31]. 3034 is an inhibitory compound that can competitively bind with Sb9 to restore the level and bioactivity of GrB. To study the efficacy of 3034-containing nanomedicine-mediated GrB restoring, the cellular level of GrB after different treatments was evaluated by western blotting. As shown in Figs. 2(g) and 2(h), 3034-containing nanomedicines, including 3L, D3L, and D3RL can effectively decrease the level of the Sb9-GrB complex, and consequently increase the level of GrB. Remarkably, compared with D3L, D3RL conducted a more effective GrB restoring (~ 2.5-fold vs. 1.8-fold), which further emphasizes the enhanced cellular uptake of RGD decoration.

2.4 Pharmacokinetics and biodistribution in vivo

The enhanced ICD-inducing and GrB-restoring effect *in vitro* prompted us to evaluate the antitumor potential of D3RL *in vivo*. Before evaluating the therapeutic effect, we first investigated the pharmacokinetics and biodistribution of D3RL. In detail, to track D3RL *in vivo*, a classical near-infrared fluorescent dye, indocyanine green (ICG) was coloaded with a similar protocol, and the obtained nanoformulations were denoted as ICG-D3L and ICG-D3RL. Free ICG, ICG-D3L, and ICG-D3RL were injected intravenously into 4T1-Luc tumor-bearing mice with an

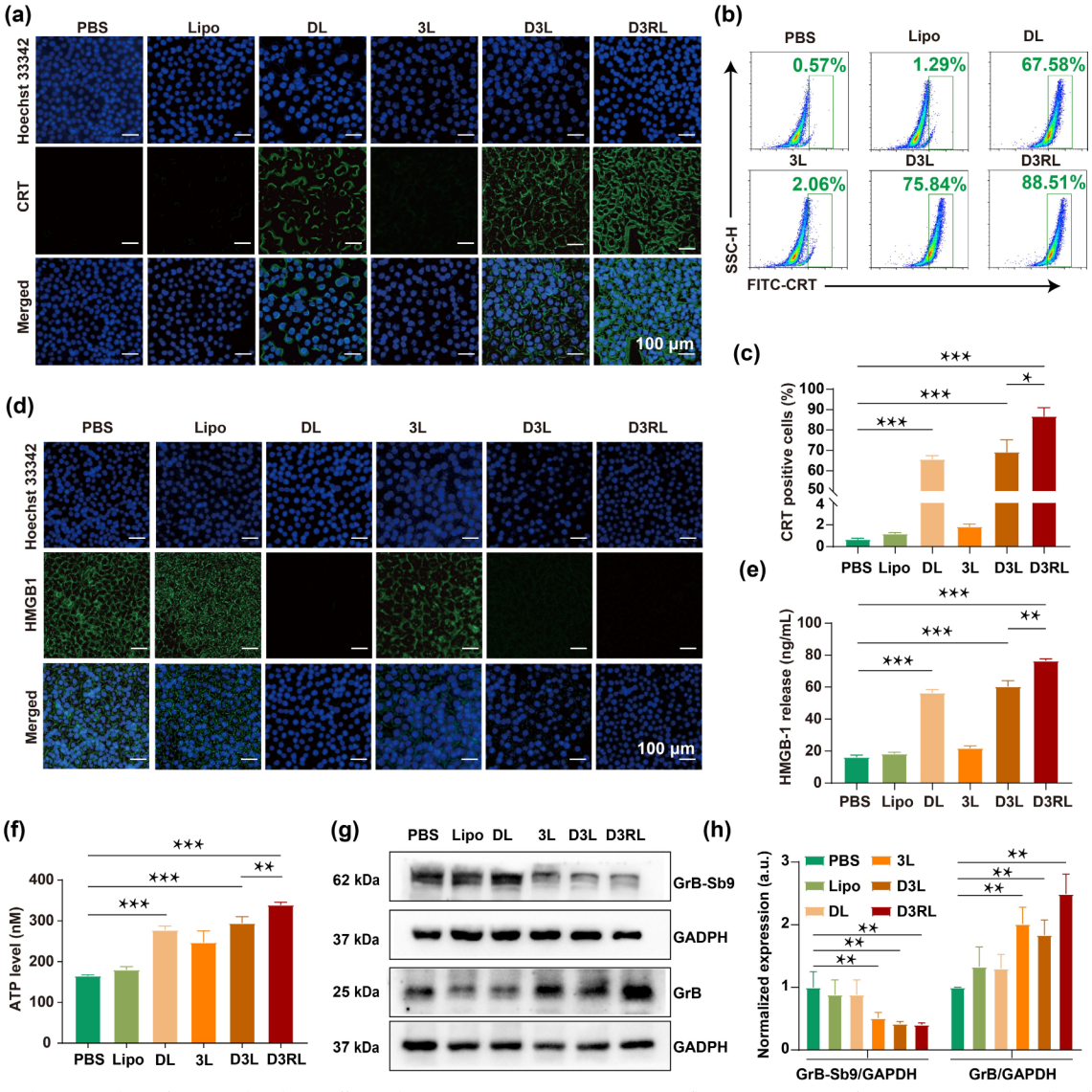

Figure 2 Mechanism analysis of D3RL induced ICD effect and GrB restoration *in vitro*. (a) Immunofluorescence images of CRT exposure on the cell surface of 4T1-Luc cells with different treatments. Scale bar, 100 μm. (b) Flow cytometry and (c) quantitative analysis of CRT-positive 4T1-Luc cells with indicated treatments. (d) Immunofluorescence images of HMGB1 released from 4T1-Luc cells with different treatments. Scale bar, 100 μm. (e) Quantitative analysis of HMGB1 release from 4T1-Luc cells with different treatments using an ELISA kit. (f) ATP secretion from 4T1-Luc cells after different treatments using an ATP assay kit. (g) Western blot analysis of 4T1-Luc cells with different treatments. (h) Statistical analysis of expression of GrB-Sb9 and GrB normalized to control. Data were analyzed by GraphPad Prism software. Student's *t*-test was performed for the statistical analysis of the two groups. Data are shown as mean ± s. d. (n = 3). *, $p < 0.05$; **, $p < 0.01$; ***, $p < 0.001$.

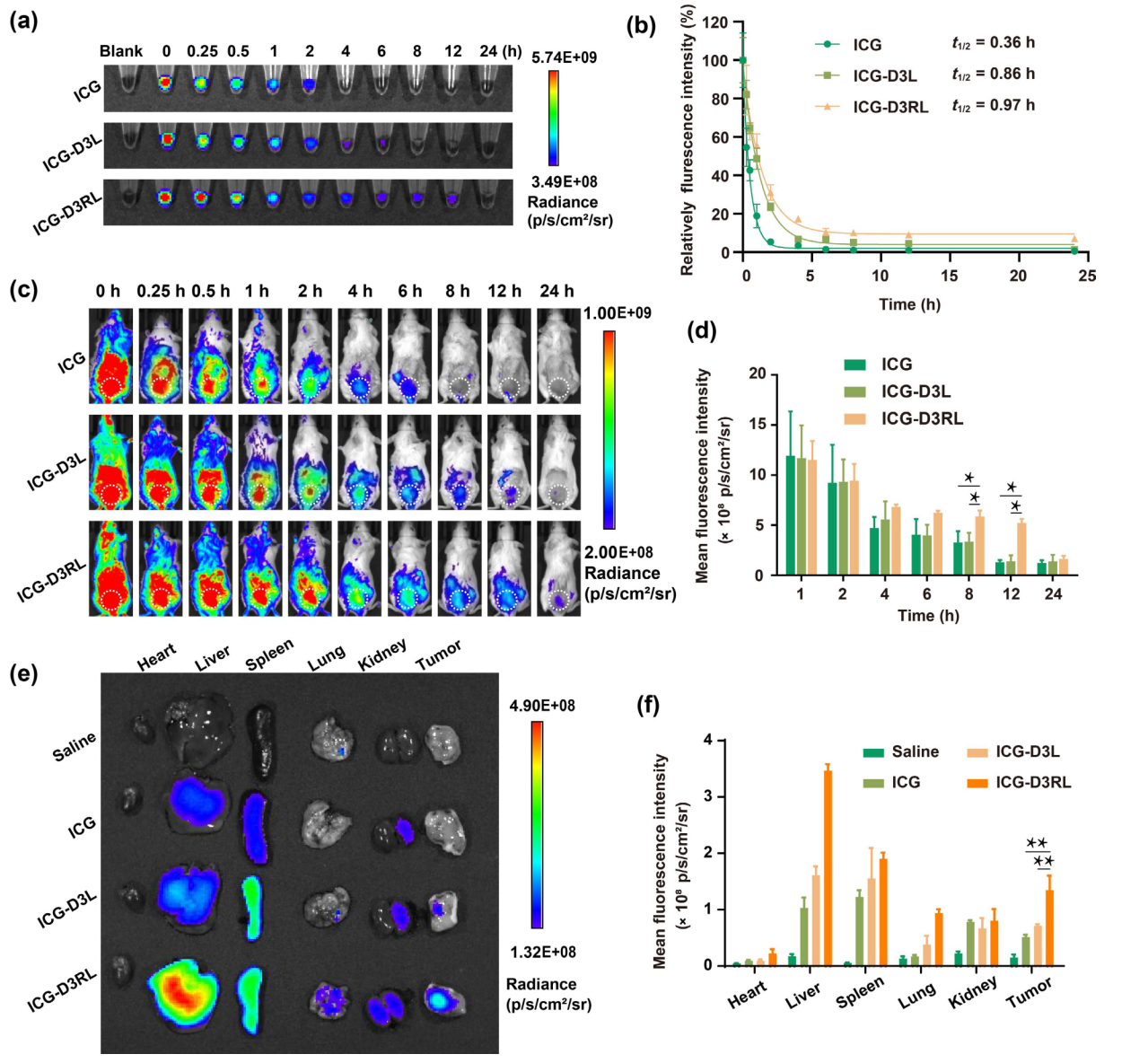

Figure 3 Pharmacokinetics and biodistribution analysis of D3RL *in vivo*. (a) Fluorescence images and (b) semi-quantitative analysis of fluorescence intensity of blood samples collected at the indicated time points derived from 4T1-Luc tumor-bearing mice injected with free ICG, ICG-labeled 3DL(ICG-3DL), or ICG-labeled D3RL (ICG-D3RL). (c) *In vivo* fluorescence imaging of 4T1-Luc tumor-bearing mice at different time points after intravenous administration of free ICG, ICG-D3L, or ICG-D3RL. Tumor regions are circled with white dashed lines. (d) Semi-quantitative analysis of fluorescence intensity of the tumor regions at different time points post-injection. (e) *Ex vivo* fluorescence images and (f) semi-quantitative analysis of fluorescence intensity of the tumors and major organs 12 h post-injection. Data were analyzed by GraphPad Prism software. Student's *t*-test was performed for the statistical analysis of the two groups. Data are shown as mean ± s. d. ($n = 3$) *, $p < 0.05$; **, $p < 0.01$.

equivalent dosage of ICG, and blood was collected from the tail vein at predetermined time points for imaging. As shown in Figs. 3(a) and 3(b), free ICG was rapidly cleared from the blood with a half-life of approximately 0.36 h. Notably, ICG-labeled nanomedicines were cleared more slowly with a half-life of more than 2-fold prolonged. *In vivo* whole-body fluorescence imaging of tumor-bearing mice also confirmed the slowest clearance rate of ICG-D3RL (Figs. 3(c) and 3(d)). *Ex vivo* imaging of excised major organs and tumors 12 h post-injection also verified the enhanced accumulation of ICG-D3RL in tumor tissues (Figs. 3(e) and 3(f)). Taken together, the developed D3RL achieved prolonged blood clearance time and effective tumor accumulation, which was favorable for therapeutic effect *in vivo*.

2.5 Antitumor effect of ORI-VGB NMs in vivo

The anti-tumor effect of D3RL was evaluated in the 4T1-Luc subcutaneous tumor model. 4T1-Luc tumor-bearing mice were intravenously injected with PBS, blank liposome (Lipo), DL, 3L, D3L, or D3RL for 5 times in the therapeutic trials (Fig. 4(a)). The growth of tumors was monitored by bioluminescence imaging. Compared with PBS and Lipo groups, both D3L and D3RL remarkably restrained the rapid tumor growth (Figs. 4(b) and 4(c)). Notably, the D3RL group exhibited a better therapeutic effect than the other groups. To quantitatively evaluate the therapeutic effect, we also measured the tumor volumes per other days in the whole treatment. As shown in Figs. 4(d) and 4(e), the tumor size increased rapidly in the PBS and Lipo groups, but 3L treatment barely inhibited tumor progress. Unlike the result of bioluminescence imaging, both DL and D3L effectively restrained tumor growth with a tumor inhibition rate (TIR) of 54.3% and 70.2%, respectively. The enhanced TIR induced by D3L may be attributed to the relief of 3034 to the host immunity. Moreover, the tumor growth was more significantly inhibited in the D3RL group with a TIR of 78.9%, which may be attributed to the enhanced tumor accumulation from RGD decoration. At the end of treatment, mice were sacrificed, and the tumors were excised

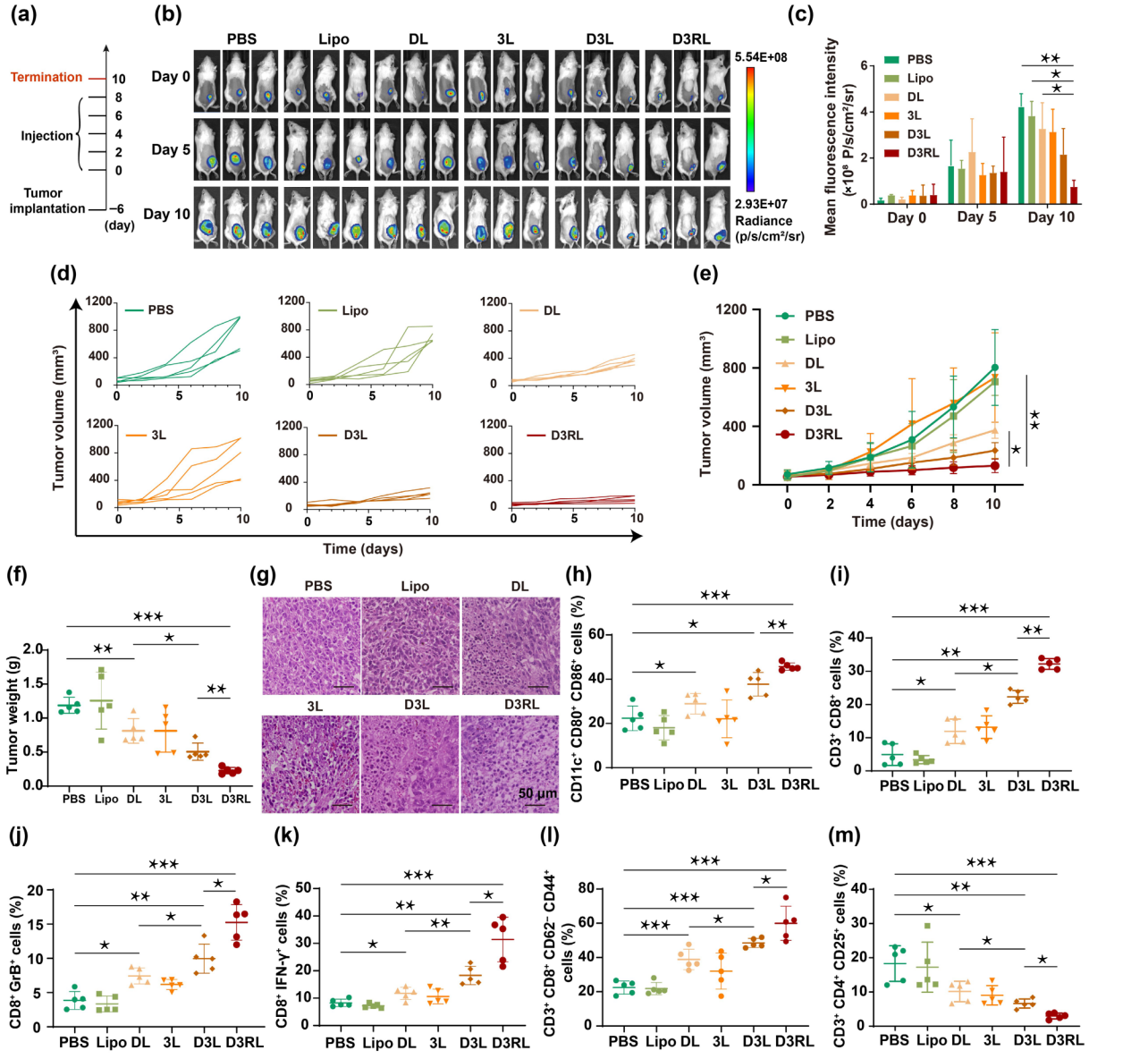

Figure 4 *In vivo* antitumor effect of D3RL. (a) Schematic illustration of the timeline for the therapeutic experiment. (b) Representative bioluminescence images and (c) semi-quantitative analysis of 4T1-Luc tumor-bearing mice during the therapeutic period. ((d) and (e)) Tumor growth curves of mice with different treatments. (f) Weights of tumors collected from mice with different treatments. (g) H&E staining of tumor sections from mice with different treatments. Scale bar, 50 μm. (h) Quantitative analysis of matured DCs in tumor-draining lymph nodes (TDLN) from mice with different treatments. (i) Quantitative analysis of infiltrated CTLs ($CD8^+$ in $CD3^+$ cells), (j) effector $CD8^+GrB^+$ T cells, (k) effector $CD8^+IFN\gamma^+$ T cells, (l) effector memory ($CD3^+CD8^+CD62L^-CD44^+$) T cells, and (m) immunosuppressive regulatory ($CD3^+CD4^+CD25^+$) T cells in tumors from mice with different treatments. Data were analyzed by GraphPad Prism software. Student's *t*-test was performed for the statistical analysis of the two groups. Data are shown as mean ± s. d. ($n = 5$). *, $p < 0.05$; **, $p < 0.01$; ***, $p < 0.001$.

and weighed. The evaluation of tumor weights was consistent with the result of *in vivo* volume measurement (Fig. 4(f)). Additionally, hematoxylin and eosin (H&E) staining results of tumors suffering from indicated treatments showed that D3RL caused the most cell death with a loose cell arrangement (Fig. 4(g)). All these results confirmed the superior antitumor effect of D3RL treatment.

To further verify the underlying immunological mechanism of prominent therapeutic efficacy provided by D3RL, tumor tissues and the tumor-draining lymph nodes were harvested at the end of the trial, and used to analyze the population of tumor-infiltrating immune cells by flow cytometry. As shown in Fig. 4(h) and Fig. S7 in the ESM, compared with the PBS group, the maturation of dendritic cells (DCs) ($CD11c^+CD80^+CD86^+$) was up-regulated after being treated with DOX-containing nanomedicines. Notably, the proportion of DC maturation in the D3RL group was much higher than DL or D3L treatment group, indicating that D3RL can effectively promote DC maturation. Furthermore, we quantitatively analyzed the proportion of infiltrating immune cells in tumor tissues from different treatment groups. As shown in Figs. 4(i)–4(l) and Figs. S8–S11 in the ESM, the proportion of total cytotoxic T cells ($CD3^+CD8^+CD4^-$), effector $CD3^+CD8^+GrB^+$ T cells, effector $CD3^+CD8^+IFN\gamma^+$ T cells, and effector memory ($CD3^+CD8^+CD62L^-CD44^+$) T cells were all significantly improved after treated with DOX-containing nanomedicines. Notably, D3L induced a more effective up-regulation than DL and the D3RL treatment leads to the best improvement of these effector T cells infiltrations. On the contrary, the level of immunosuppressive regulatory T cells ($CD3^+CD4^+CD25^+$) was significantly lower in tumor tissues from the D3RL-treatment group, as compared with other groups (Fig. 4(m) and Fig. S12 in the ESM). Taken together, D3RL can effectively activate the host immune response of 4T1-Luc tumor-bearing mice and elevate the populations of infiltrated cytotoxic immune cells in tumor tissue.

Besides, to further understand the improved infiltration of cytotoxic immune cells, tumor sections from mice with different treatments were subjected to histopathological examination.

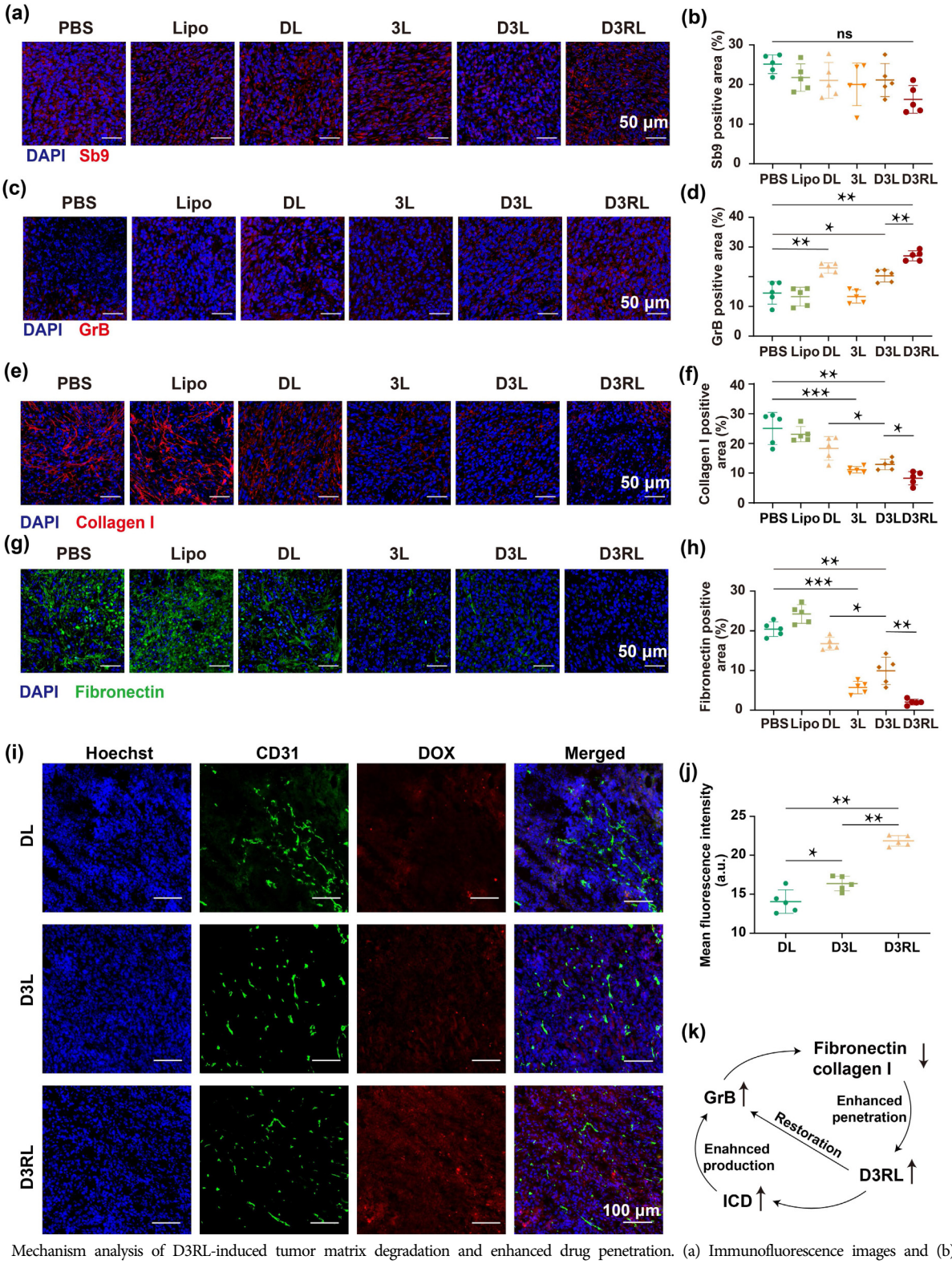

Figure 5 Mechanism analysis of D3RL-induced tumor matrix degradation and enhanced drug penetration. (a) Immunofluorescence images and (b) semi-quantitative analysis of Sb9 expression in 4T1-Luc tumors with different treatments. Scale bar, 50 μm. (c) Immunofluorescence images and (d) semi-quantitative analysis of GrB expression in 4T1-Luc tumors with different treatments. Scale bar, 50 μm. (e) Immunofluorescence images and (f) semi-quantitative analysis of collagen I expression in 4T1-Luc tumors with different treatments. Scale bar, 50 μm. (g) Immunofluorescence images and (h) semi-quantitative analysis of fibronectin expression in 4T1-Luc tumors with different treatments. Scale bar, 50 μm. (i) immunofluorescence images of tumor sections from mice with different treatments. Blood vessels were stained with CD31 (green) and nuclei were stained with Hoechst 33342 (blue). Scale bar, 100 μm. (j) Quantitative analysis of the average fluorescence signal intensity of DOX (red) in the tumor sections. (k) Schematic diagram of D3RL-induced tumor matrix degradation and enhanced drug penetration. Data were analyzed by GraphPad Prism software. Student's *t*-test was performed for the statistical analysis of the two groups. Data are shown as mean ± s. d. ($n = 5$). *, $p < 0.05$; **, $p < 0.01$; ***, $p < 0.001$; ns, no significance.

Further immunofluorescence staining of Sb9 revealed that D3RL had a negligible effect on the expression level of Sb9 (Figs. 5(a) and 5(b)). On the contrary, D3RL significantly promoted the expression level of GrB (Figs. 5(c) and 5(d)), which may be attributed to the effective ICD inducing, as well as GrB restoring by D3RL. Considering the well-reported degradation effect of GrB on the matrix component [16], we further evaluated the level of the matrix (for example, collagen I and fibronectin) on the tumor

tissues from different groups. As shown in Figs. 5(e)–5(h), 3034-containing nanomedicines effectively reduced the level of collagen I and fibronectin. The enhanced matrix degradation was attributed to the restoration effect of 3034 to infiltrated GrB in the tumor microenvironment. Notably, the D3RL exhibited a more effective degradation of collagen I and fibronectin than the other treatment. Based on the prominent matrix degradation effect of D3RL, we further analyzed the penetration of nanomedicines at the end of trials. Dox-containing nanomedicines were self-labeled by the red fluorescence of DOX. As shown in Figs. 5(i) and 5(j), compared with the DL treatment group, tumor sections from the D3L group exhibited more fluorescence signals of DOX. As expectedly, the D3RL-treated groups showed the strongest signal of DOX, verifying the enhanced drug penetration induced by D3RL, which was consistent with the results of matrix degradation above. Above all, D3RL effectively induced tumor matrix degradation and consequently enhanced the penetration of nanomedicines, which in return further promoted the production and restoration of GrB (Fig. 5(k)).

To evaluate any potential adverse effects of D3RL-mediated therapy, the body weights of mice during the trials were monitored. As shown in Fig. S13 in the ESM, negligible body-weight changes were observed during the treatment periods. Furthermore, no obvious disruption of cardiac, hepatic, or renal function was detected after treatment according to the serum biochemical analysis (Fig. S14 in the ESM). The histomorphology examination of major organs (including heart, liver, spleen, lung, and kidney) by H&E staining exhibited barely any pathological changes at the end of treatments (Fig. S15 in the ESM), supporting the biosafety of D3RL-mediated chemo-immunotherapy.

3 Conclusion

In summary, the development of DOX and 3034 coloaded tumor targeting nanomedicine, D3RL, has shown promising results in the treatment of breast cancer through a combination of chemo-immunotherapy. The nanomedicine accumulates at the tumor site, releasing DOX to directly kill tumor cells and activate the host immune response through induction of ICD. Additionally, the locally released 3034 relieves the inhibition of Sb9 on GrB, leading to the degradation of matrix components and enhancing the infiltration of immune cells and nanomedicine penetration, which in return resulting in an improved therapeutic outcome. This work represents a novel and effective approach for the targeted production and restoration of GrB in breast cancer treatment with minimal side effects.

Acknowledgments

The authors thank Prof. Fazhan Wang (the First Affiliated Hospital, Zhengzhou University) and Prof. Bing Jiang (Nanozyme Medical Center, Zhengzhou University) for assistance with the histological examination and bioimaging *in vivo* and *ex vivo*. The authors also thank the center of Advanced Analysis & Gene Sequencing, Zhengzhou University for technical assistance. This work was supported by grants from the National Natural Science Foundation of China (Nos. 32000998, and 32201240). The Young Elite Scientists Sponsorship Program by Henan Association for Science and Technology (No. 2022HYTP046), the China Postdoctoral Science Foundation (Nos. 2019TQ0285, 2019M662513, and 2021TQ0298), Henan provincial Medical Science and Technology Research Project (No. LHGJ20210210), and Science and Technology Development Project of Henan Province (Nos. 212102310138 and 222102310525).

Electronic Supplementary Material: Supplementary material (materials and methods, instruments and characterization, summary of zeta potentials and hydrodynamic size, mass spectrum analysis, loading efficiency, encapsulation efficiency of drugs, TEM images and hydrodynamic size distribution, storage stability evaluation, cytotoxic evaluation, flow cytometry gating strategies, body weights of mice, serum biochemistry analysis, and H&E staining histological images) is available in the online version of this article at https://doi.org/10.1007/s12274-023-5581-6.

References

[1] Giaquinto, A. N.; Sung, H.; Miller, K. D.; Kramer, J. L.; Newman, L. A.; Minihan, A.; Jemal, A.; Siegel, R. L. Breast cancer statistics, 2022. *CA Cancer J. Clin.* **2022**, *72*, 524–541.

[2] Kroemer, G.; Senovilla, L.; Galluzzi, L.; André, F.; Zitvogel, L. Natural and therapy-induced immunosurveillance in breast cancer. *Nat. Med.* **2015**, *21*, 1128–1138.

[3] Barnestein, R.; Galland, L.; Kalfeist, L.; Ghiringhelli, F.; Ladoire, S.; Limagne, E. Immunosuppressive tumor microenvironment modulation by chemotherapies and targeted therapies to enhance immunotherapy effectiveness. *OncoImmunology* **2022**, *11*, 2120676.

[4] Wen, Y. Y.; Chen, X.; Zhu, X. F.; Gong, Y. C.; Yuan, G. L.; Qin, X. Y.; Liu, J. Photothermal-chemotherapy integrated nanoparticles with tumor microenvironment response enhanced the induction of immunogenic cell Death for colorectal cancer efficient treatment. *ACS Appl. Mater. Interfaces* **2019**, *11*, 43393–43408.

[5] Zhao, X.; Yang, K. N.; Zhao, R. F.; Ji, T. J.; Wang, X. C.; Yang, X.; Zhang, Y. L.; Cheng, K. M.; Liu, S. L.; Hao, J. H. et al. Inducing enhanced immunogenic cell death with nanocarrier-based drug delivery systems for pancreatic cancer therapy. *Biomaterials* **2016**, *102*, 187–197.

[6] Chen, Y.; Zeng, L. Y.; Zhu, H. Z.; Wu, Q. F.; Liu, R.; Liang, Q.; Chen, B.; Dai, H. T.; Tang, K. Y.; Liao, C. L. et al. Ferritin nanocaged doxorubicin potentiates chemo-immunotherapy against hepatocellular carcinoma via immunogenic cell death. *Small Methods* **2022**, 2201086.

[7] Zhang, B. L.; Chen, X. H.; Tang, G. H.; Zhang, R. F.; Li, J. Y.; Sun, G. M.; Yan, X. Y.; Fan, K. L. Constructing a nanocage-based universal carrier for delivering TLR-activating nucleic acids to enhance antitumor immunotherapy. *Nano Today* **2022**, *46*, 101564.

[8] Wang, K. W.; Jiang, M. L.; Zhou, J. L.; Liu, Y.; Zong, Q. Y.; Yuan, Y. Y. Tumor-acidity and bioorthogonal chemistry-mediated on-site size transformation clustered nanosystem to overcome hypoxic resistance and enhance chemoimmunotherapy. *ACS Nano* **2022**, *16*, 721–735.

[9] Wang, Q.; Ju, X. L.; Wang, J. Y.; Fan, Y.; Ren, M. J.; Zhang, H. Immunogenic cell death in anticancer chemotherapy and its impact on clinical studies. *Cancer Lett.* **2018**, *438*, 17–23.

[10] Jin, S. M.; Lee, S. N.; Kim, J. E.; Yoo, Y. J.; Song, C.; Shin, H. S.; Phuengkham, H.; Lee, C. H.; Um, S. H.; Lim, Y. T. Overcoming chemoimmunotherapy-induced immunosuppression by assemblable and depot forming immune modulating nanosuspension. *Adv. Sci.* **2021**, *8*, 2102043.

[11] Tibbs, E.; Cao, X. F. Emerging canonical and non-canonical roles of granzyme B in health and disease. *Cancers* **2022**, *14*, 1436.

[12] Xu, L. L.; Liu, N. H.; Zhan, W. J.; Deng, Y.; Chen, Z. X.; Liu, X. Y.; Gao, G.; Chen, Q.; Liu, Z.; Liang, G. L. Granzyme B turns nanoparticle fluorescence "On" for imaging cytotoxic T lymphocyte activity *in vivo*. *ACS Nano* **2022**, *16*, 19328–19334.

[13] Nüssing, S.; Sutton, V. R.; Trapani, J. A.; Parish, I. A. Beyond target cell death-Granzyme serine proteases in health and disease. *Mol. Aspects Med.* **2022**, *88*, 101152.

[14] Han, R.; Yu, L. T.; Zhao, C. X.; Li, Y.; Ma, Y. Y.; Zhai, Y. W.; Qian, Z. Y.; Gu, Y. Q.; Li, S. W. Inhibition of SerpinB9 to enhance granzyme B-based tumor therapy by using a modified biomimetic nanoplatform with a cascade strategy. *Biomaterials* **2022**, *288*, 121723.

[15] Ibáñez-Molero, S.; van Vliet, A.; Pozniak, J.; Hummelink, K.; Terry,

A. M.; Monkhorst, K.; Sanders, J.; Hofland, I.; Landeloos, E.; Van Herck, Y. et al. *SERPINB9* is commonly amplified and high expression in cancer cells correlates with poor immune checkpoint blockade response. *OncoImmunology* **2022**, *11*, 2139074.

[16] Velotti, F.; Barchetta, I.; Cimini, F. A.; Cavallo, M. G. Granzyme B in Inflammatory diseases: Apoptosis, inflammation, extracellular matrix remodeling, epithelial-to-mesenchymal transition and fibrosis. *Front. Immunol.* **2020**, *11*, 587581.

[17] Rauner, G.; Kuperwasser, C. Microenvironmental control of cell fate decisions in mammary gland development and cancer. *Dev. Cell* **2021**, *56*, 1875–1883.

[18] Jiang, L. W.; Wang, Y. J.; Zhao, J.; Uehara, M.; Hou, Q. M.; Kasinath, V.; Ichimura, T.; Banouni, N.; Dai, L. et al. Direct tumor killing and immunotherapy through anti-SerpinB9 therapy. *Cell* **2020**, *183*, 1219–1233.e18.

[19] Hirst, C. E.; Buzza, M. S.; Bird, C. H.; Warren, H. S.; Cameron, P. U.; Zhang, M. L.; Ashton-Rickardt, P. G.; Bird, P. I. The intracellular granzyme B inhibitor, proteinase inhibitor 9, is up-regulated during accessory cell maturation and effector cell degranulation, and its overexpression enhances CTL potency. *J. Immunol.* **2003**, *170*, 805–815.

[20] Lan, Y.; Liang, Q. W.; Sun, Y.; Cao, A. C.; Liu, L.; Yu, S. Y.; Zhou, L. Y.; Liu, J. X.; Zhu, R. Y.; Liu, Y. H. Codelivered chemotherapeutic doxorubicin via a dual-functional immunostimulatory polymeric prodrug for breast cancer immunochemotherapy. *ACS Appl. Mater. Interfaces* **2020**, *12*, 31904–31921.

[21] Lee, N. K.; Choi, J. U.; Kim, H. R.; Chung, S. W.; Ko, Y. G.; Cho, Y. S.; Park, S. J.; Lee, E. J.; Kim, S. Y.; Kim, I. S. et al. Caspase-cleavable peptide-doxorubicin conjugate in combination with CD47-antagonizing nanocage therapeutics for immune-mediated elimination of colorectal cancer. *Biomaterials* **2021**, *277*, 121105.

[22] Choi, J.; Shim, M. K.; Yang, S.; Hwang, H. S.; Cho, H.; Kim, J.; Yun, W. S.; Moon, Y.; Kim, J.; Yoon, H. Y. et al. Visible-light-triggered prodrug nanoparticles combine chemotherapy and photodynamic therapy to potentiate checkpoint blockade cancer immunotherapy. *ACS Nano* **2021**, *15*, 12086–12098.

[23] Qiu, M.; Sun, H. L.; Meng, F. H.; Cheng, R.; Zhang, J.; Deng, C.; Zhong, Z. Y. Lipopepsomes: A novel and robust family of nano-vesicles capable of highly efficient encapsulation and tumor-targeted delivery of doxorubicin hydrochloride *in vivo*. *J. Controlled Release* **2018**, *272*, 107–113.

[24] Wu, J. R.; Meng, Z. Y.; Exner, A. A.; Cai, X. J.; Xie, X.; Hu, B.; Chen, Y.; Zheng, Y. Y. Biodegradable cascade nanocatalysts enable tumor-microenvironment remodeling for controllable CO release and targeted/synergistic cancer nanotherapy. *Biomaterials* **2021**, *276*, 121001.

[25] Zhang, Y. L.; Wei, J. Y.; Liu, S. L.; Wang, J.; Han, X. X.; Qin, H.; Lang, J. Y.; Cheng, K. M.; Li, Y. Y.; Qi, Y. Q. et al. Inhibition of platelet function using liposomal nanoparticles blocks tumor metastasis. *Theranostics* **2017**, *7*, 1062–1071.

[26] Wang, L.; Niu, X. X.; Song, Q. L.; Jia, J. J.; Hao, Y. W.; Zheng, C. X.; Ding, K. L.; Xiao, H. F.; Liu, X. X.; Zhang, Z. Z. et al. A two-step precise targeting nanoplatform for tumor therapy via the alkyl radicals activated by the microenvironment of organelles. *J. Controlled Release* **2020**, *318*, 197–209.

[27] Zhang, L. J.; Qi, Y. Q.; Min, H.; Ni, C.; Wang, F.; Wang, B.; Qin, H.; Zhang, Y. L.; Liu, G. N.; Qin, Y. et al. Cooperatively responsive peptide nanotherapeutic that regulates angiopoietin receptor tie2 activity in tumor microenvironment to prevent breast tumor relapse after chemotherapy. *ACS Nano* **2019**, *13*, 5091–5102.

[28] Manzari, M. T.; Shamay, Y.; Kiguchi, H.; Rosen, N.; Scaltriti, M.; Heller, D. A. Targeted drug delivery strategies for precision medicines. *Nat. Rev. Mater.* **2021**, *6*, 351–370.

[29] Wang, Z. R.; Zhang, S.; Zhang, R. F.; Chen, X. H.; Sun, G. M.; Zhou, M.; Han, Q. B.; Zhang, B. L.; Zhao, Y.; Jiang, B. et al. Bioengineered dual-targeting protein nanocage for stereoscopical loading of synergistic hydrophilic/hydrophobic drugs to enhance anticancer efficacy. *Adv. Funct. Mater.* **2021**, *31*, 2102004.

[30] Han, X. X.; Cheng, K. M.; Xu, Y.; Wang, Y. Z.; Min, H.; Zhang, Y. L.; Zhao, X.; Zhao, R. R.; Anderson, G. J.; Ren, L. et al. Modularly designed peptide nanoprodrug augments antitumor immunity of PD-L1 checkpoint blockade by targeting indoleamine 2, 3-dioxygenase. *J. Am. Chem. Soc.* **2020**, *142*, 2490–2496.

[31] Medema, J. P.; de Jong. J.; Peltenburg, L. T. C.; Verdegaal, E. M. E.; Gorter, A.; Bres, S. A.; Franken, K. L. M. C.; Hahne, M.; Albar, J. P.; Melief, C. J. M. et al. Blockade of the granzyme B/perforin pathway through overexpression of the serine protease inhibitor PI-9/SPI-6 constitutes a mechanism for immune escape by tumors. *Proc. Natl. Acad. Sci. USA* **2001**, *98*, 11515–11520.